Skeletal Octahedral Nanoframe with Cartesian Coordinates *via* Geometrically Precise Nanoscale Phase Segregation in a Pt@Ni Core–Shell Nanocrystal

Aram Oh,[†,‡] Hionsuck Baik,[§,▽] Dong Shin Choi,[⊥,▽] Jae Yeong Cheon,[∥,▽] Byeongyoon Kim,[†,‡] Heejin Kim,[⊥] Seong Jung Kwon,[#] Sang Hoon Joo,[*,∥,¶] Yousung Jung,[*,⊥] and Kwangyeol Lee[*,†,‡]

[†]Center for Molecular Spectroscopy and Dynamics, Institute for Basic Science (IBS), and [‡]Department of Chemistry and Research Institute for Natural Sciences, Korea University, Seoul 136-713, Republic of Korea, [§]Korea Basic Science Institute (KBSI), Seoul 136-713, Republic of Korea, [⊥]Graduate School of Energy Environment Water and Sustainability (EEWS), Korea Advanced Institute of Science and Technology (KAIST), Daejeon 305-701, Republic of Korea, [∥]Department of Chemistry and [¶]School of Energy and Chemical Engineering, Ulsan National Institute of Science and Technology (UNIST), Ulsan 689-798, Republic of Korea, and [#]Department of Chemistry, Konkuk University, Seoul 143-701, Republic of Korea. [▽]H. Baik, D. S. Choi, and J. Y. Cheon contributed equally to this work.

ABSTRACT Catalytic properties of nanoparticles can be significantly enhanced by controlling nanoscale alloying and its structure. In this work, by using a facet-controlled Pt@Ni core–shell octahedron nanoparticle, we show that the nanoscale phase segregation can have directionality and be geometrically controlled to produce a Ni octahedron that is penetrated by Pt atoms along three orthogonal Cartesian axes and is coated by Pt atoms along its edges. This peculiar anisotropic diffusion of Pt core atoms along the ⟨100⟩ vertex, and then toward the ⟨110⟩ edges, is explained *via* the minimum strain energy for Ni–Ni pair interactions. The selective removal of the Ni-rich phase by etching then results in structurally fortified Pt-rich skeletal PtNi alloy framework nanostructures. Electrochemical evaluation of this hollow nanoframe suggests that the oxygen reduction reaction (ORR) activity is greatly improved compared to conventional Pt catalysts.

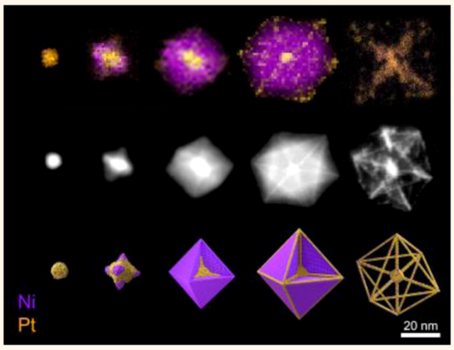

KEYWORDS: platinum · nanoparticles · crystal growth · alloy · phase segregation

Fuel cell electrode performance has been greatly improved by recent advances in the synthesis of platinum-based alloy nanocatalysts.[1−11] Nanoscale phase segregation, resulting from the rearrangement of atom positions in alloy nanoparticles, has been linked to the improvement of electrocatalytic performance in catalytic applications.[12−15] Therefore, such phenomena have been actively pursued to prepare better-performing nanocatalysts. Thermal treatment, chemical etching, ion exchange, and surface binding of small molecules have been particularly useful in inducing the desired nanoscale phase segregation.[16−20] Ultimately, the ability to control the precise atomic compositions of the alloy nanoparticles in a three-dimensional fashion would be highly desirable.

One essential feature required to achieve the latter goal is to control directionality of the phase segregation to create nanostructures with the desired atoms in the desired positions such as the facet center, edge, or vertex locations of facet-controlled alloy nanoparticles. This would then yield compositional heterogeneity on the surface of the alloy nanoparticle, potentially with enhanced catalytic properties.[15,21−23] The directional movements of the constituting atoms may be accomplished even within the matrix of a facet-controlled alloy nanoparticle using the well-differentiated morphology-dependent nanoparticle surface energetics.[19]

In order to prove our concept, we studied the carbon monoxide (CO)-induced phase segregation within an *in situ* formed facet-controlled octahedral Pt@Ni core–shell nanoparticle with Ni as the dominant component; by using Pt as the minor component, the localization of Pt can be easily

* Address correspondence to
kylee1@korea.ac.kr;
ysjn@kaist.ac.kr;
shjoo@unist.ac.kr.

Received for review December 2, 2014
and accepted March 3, 2015.

10.1021/nn5068539

visualized by the high-angle annular dark-field scanning transmission electron microscopy (HAADF-STEM) technique. We found that CO-induced phase segregation within a facet-controlled octahedral Pt@Ni nanoparticle forms a novel, geometrically highly symmetric phase-segregated PtNi nanostructure, in which a Ni octahedron is encased by an octahedral framework of Pt and is further fortified with three intersecting, perpendicular Pt axes. The underlying mechanism of this intriguing anisotropic nanoscale phase segregation phenomenon can be understood *via* strain energy minimization. While nanoscale phase segregation has been previously observed for a PtNi binary nanoparticle and other binary systems,[19,20,23−25] the preciseness of the phase segregation with the high symmetry and complexity found in this study is totally unprecedented. Also, the nanoscale phase segregation process can now be explained by both a novel visualization of the atomic diffusion paths and an energy calculation. We also found that the nanoframe structures derived from the geometrically precisely phase-segregated nanoparticles had excellent catalytic properties for the oxygen reduction reaction.

RESULTS AND DISCUSSION

In a typical synthesis of a phase-segregated octahedral PtNi nanoparticle (PON; $Pt_{0.03}Ni_{0.97}$; see Supporting Information Figure S1 for the elemental analysis; all abbreviations for synthesized nanoparticles are summarized in Table 1), a mixture of Pt(II) acetylacetonate, Ni(II) acetylacetonate, stearic acid, and octadecylamine was heated at 170 °C under 1 atm of CO for 5 h. The CO molecule acted as both the reducing agent and surface stabilization agent for the nanoparticle morphological generation, as also shown by other examples.[26] The transmission electron microscopy (TEM) and high-resolution transmission electron microscopy (HRTEM) images of a PON are shown in Figure 1. The octahedral Ni nanoparticle is enclosed by eight {111}Ni facets, forming an octahedron, and the average size of the particle is 36 ± 2 nm (Supporting Information Figure S2). The STEM image in Figure 1a exhibits vivid white lines along the inner axes and some edges of an octahedron, which were found to be Pt-rich regions by energy-dispersive X-ray spectroscopy (EDS) elemental mapping analysis (Figure 1b). In addition to the Pt localization along the ⟨110⟩ edge, the formation of three orthogonal Pt axes within the PON is also revealed by the STEM image and elemental mapping. Such geometrically precise phase segregation within a nanoparticle matrix is very rare.[24] The HRTEM image reveals a mismatch boundary at 5 or 6 layers from the surface of the {111} facet (Figure 1d-i). The (111) lattice plane spacing in this region is measured as 2.26 Å, which is about 10% more than that (2.03 Å) of inner Ni-rich phase (Figure 1d-ii). In order to show quantitatively this increase, an HRTEM strain map and profile were obtained using the geometric phase analysis (GPA) method, which confirmed also the increase of ~10% (Supporting Information Figure S3).

TABLE 1. Abbreviations for Synthesized Nanoparticles

nanomaterial	abbreviation
phase-segregated octahedral PtNi nanoparticle	PON
phase-segregated hierarchical PtNi nanoparticle	PHN
octahedral skeletal Pt-based nanoparticle	OSN
hierarchical skeletal Pt-based nanoparticle	HSN
Pt overgrowth on octahedral skeletal Pt-based nanoparticle	OSN_OV
Pt overgrowth on hierarchical skeletal Pt-based nanoparticle	HSN_OV
carbon-supported octahedral skeletal Pt-based nanoparticle	OSN/C
carbon-supported hierarchical skeletal Pt-based nanoparticle	HSN/C
carbon-supported Pt overgrown octahedral skeletal Pt-based nanoparticle	OSN_OV/C

Although it is known that CO binding can induce the surface confinement of metal atoms with strong M−CO bonds on the alloy nanoparticles *via* diffusion processes,[2,26,27] the present observation of directional confinement of a metal component at geometrically precise locations within an alloy nanoparticle has not been reported. In order to understand the formation mechanism of the three inner axes *via* nanoscale phase segregation, temporal images of the reaction intermediates were examined as shown in Figure 2. Initially small, geometrically poorly defined Pt-rich PtNi alloy, likely Pt/Ni solid solution, nanocrystals are formed (Figure 2b,f), which are gradually transformed into slightly concave Pt@Ni octahedral nanoparticles (Figure 2c,g). Then, the growth of the Ni phase follows, resulting in the formation of an octahedral core−shell Pt@Ni nanoparticle (Figure 2d,h). Close examination of the intermediates reveals the same crystal growth directions and structural motifs for both the Pt-rich inner concave octahedral nanoparticle and the final phase-segregated octahedral nanoparticle (Figure 2e,i). Therefore, the shape control of the predominantly Ni-based octahedral nanoparticle seems to be assisted by the octahedron-shaped Pt@Ni concave nanocrystal seed. Once the Ni phase starts to grow, the concave nature of the nanocrystal disappears due to the {111}Ni facet stabilization by CO.[11,28] The protruding ends of the seed Pt-rich concave nanoparticle might continue to grow during the entire nanoparticle growth process by selectively recruiting Pt precursors over Ni precursors. This would leave the Pt-rich phase along the path, which the vertices along the ⟨100⟩ direction of the octahedron pass through during the nanocrystal growth. While the above discussion seems to be in agreement with the observed product formation pattern, the three inner Pt-rich axes and ⟨110⟩ edge-coating Pt lines are not clearly visible at the reaction time of 1 h, at which point there is no further increase in the overall crystal size. Prolonged heating of the Pt@Ni nanoparticle under CO is an absolute

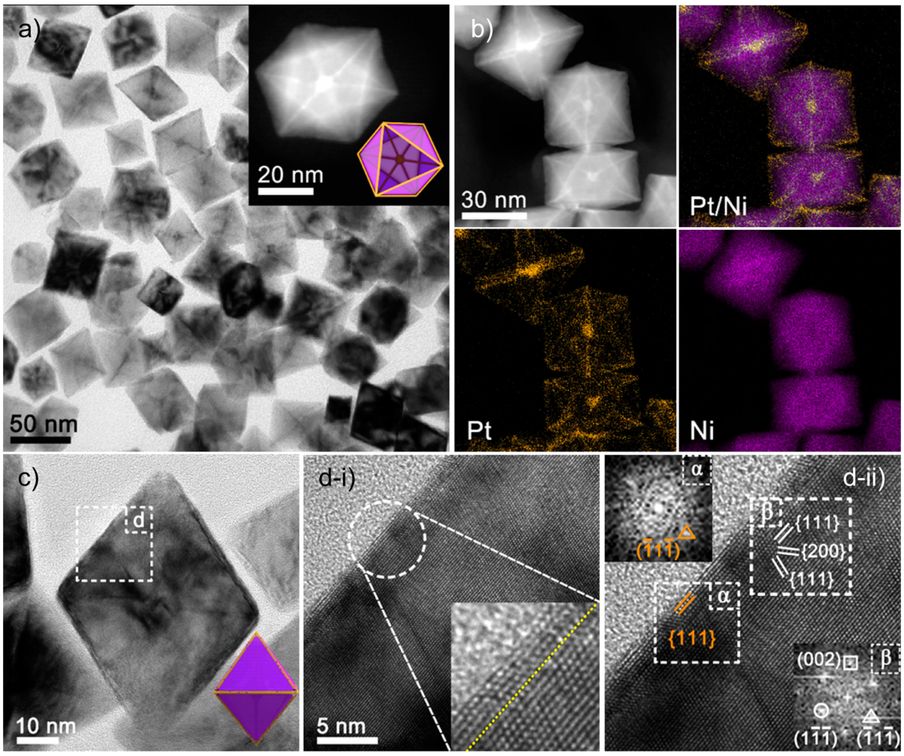

Figure 1. Structural analysis of a PON. (a) TEM image and HAADF-STEM image with a corresponding inset PON model. (b) EDS elemental mapping analysis of a PON, which shows the phase segregation between Pt (orange) and Ni (purple) components. (c, d) TEM and HRTEM images of a PON along the ⟨110⟩ zone axis. (d-i) In the edge of the PON, the mismatch boundary from the surface of the (111) facet was confirmed by spatial analysis. (d-ii) The orange and white marks in the HRTEM image represent Pt (d_{111} = 2.26 Å) and Ni (d_{111} = 2.03 Å, d_{200} = 1.76 Å), respectively.

requirement for producing Pt-rich lines along the ⟨110⟩ edges and the three perpendicular inner axes (Figure 2m). The intermediate structures between structures in Figure 2l and m are also shown in Supporting Information Figure S4.

As shown in Figure 2n–q, the EDS line profile analysis for various reaction intermediates is performed to identify the composition distribution change of the Pt and Ni components. Line scanning for the nanoparticles that do not exhibit a core–shell structure was performed along an arbitrary direction, while the nanoparticles with a core–shell structure were scanned along the ⟨110⟩ direction, which passes through the center of the nanostructure. Most strikingly, the core Pt component migrates to the surface ⟨110⟩ edges, as judged by the decrease in the size of the Pt-rich core over time (Supporting Information Figure S5). The size of the Pt-rich core, which was originally 15 ± 1 nm, was reduced to 8 ± 1 nm in the final phase-segregated nanostructure. As demonstrated by the temporal elemental mappings, the decomposition rates of the Pt precursors and the Ni precursors are greatly dissimilar (Figure 2j–m). Because the amount of fast decomposing Pt precursors in the reaction mixture would be very small in the later stage of nanocrystal growth, the amount of Pt found at the ⟨110⟩ edges of the octahedron would be very small in the absence of Pt migration from the core. The presence of CO on the nanooctahedron surface helped the movement of the Pt content from the inner Pt core to the octahedron vertices along the ⟨100⟩ directions.[29] The Pt rich ⟨110⟩ edges might have resulted from the CO-assisted Pt migration from the Pt-doped Ni matrix underneath the {111}Ni facet as well as redistribution of the Pt phase transferred from the ⟨100⟩ vertices.

An interesting morphological development was observed when the CO atmosphere was switched to Ar during the reaction (Supporting Information Figure S6). The overall nanoparticle shape takes on a concave cube-like morphology. The elemental mapping of the concave cube indicates that the Pt-rich phase is confined to the central part of the nanoparticle. No surface Pt-rich edge lines are observed due to the lack of CO-induced directional Pt migration from the core to the surface, corroborating the CO-induced Pt surface confinement process as proposed above. Furthermore, the cube-like morphology under Ar indicates the role of CO in stabilizing the {111}Ni facets.

To understand the effects of the CO ligand in promoting phase segregation and the preferential diffusion along the three Cartesian coordinate directions, we performed density functional theory (DFT) calculations and theoretical analysis. In a typical bimetallic system, the metal with the larger atomic radius and the smaller surface energy tends to segregate on

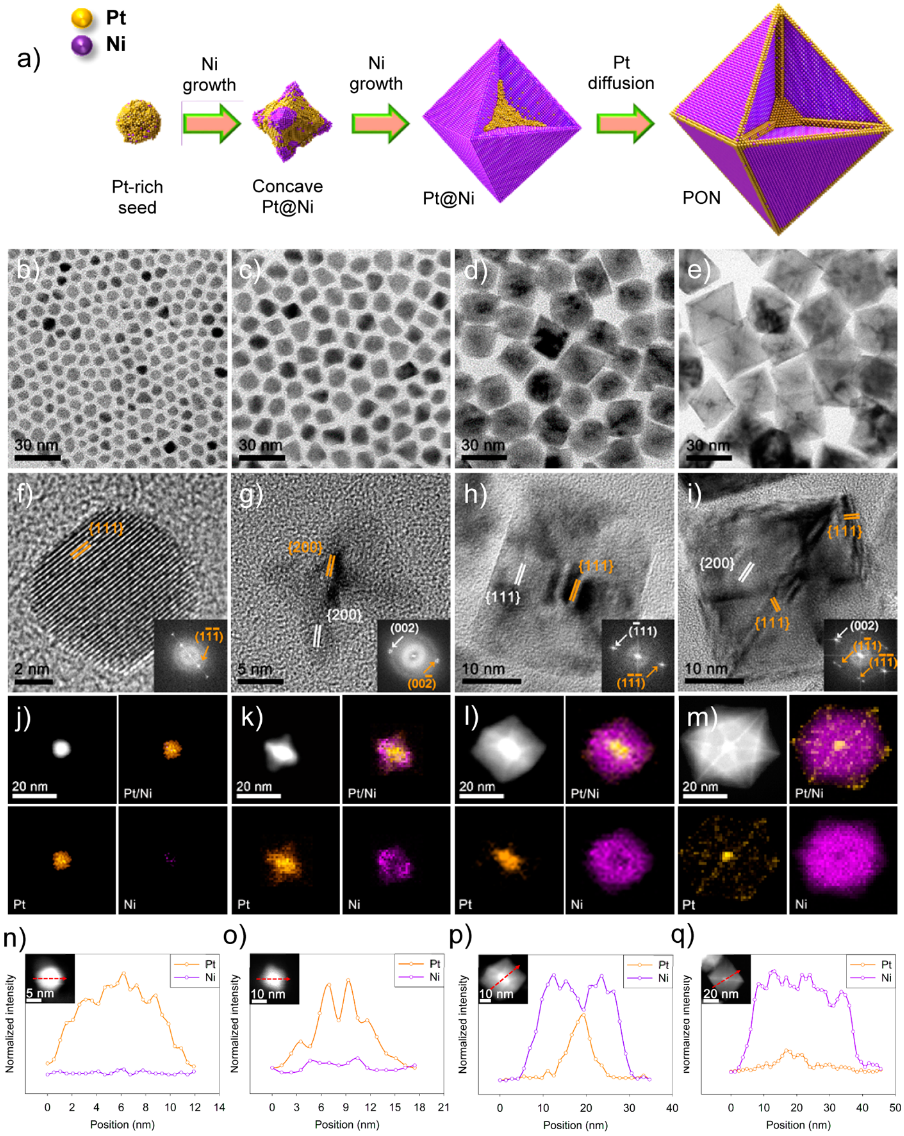

Figure 2. Structure and component analysis of a PON at different reaction times. (a) Schematic illustration for the structural evolution into a PON. TEM, HRTEM, EDS elemental mapping, and line profile images of intermediates at different reaction times of (b, f, j, n) 25 min, (c, g, k, o) 35 min, (d, h, l, p) 60 min, and (e, i, m, q) 300 min. (b−e) TEM images show shape changing in the overall synthetic process of the nanostructure, and (f−i) HRTEM with FFT images along the ⟨110⟩ zone axis confirms the phase segregation between Pt and Ni components through spatial resolution analysis. (j−m) Elemental mapping and (n−q) line profile images demonstrate the change of Pt (orange) and Ni (purple) component distributions under the synthetic process. The orange and white marks in the HRTEM images represent Pt and Ni, respectively (Pt, d_{111} = 2.26 Å, d_{200} = 1.96 Å, and Ni, d_{111} = 2.03 Å, d_{200} = 1.76 Å). Also, the red arrows in the insets of line profile images indicate line scan directions for the corresponding nanoparticles.

the surface to minimize the energy penalties arising from the strain and the unsaturated coordination, respectively. For Pt−Ni alloys, the surface energies are similar (2.475 J/m^2 for Pt (111), 2.450 J/m^2 for Ni (111)); however the atomic size difference (1.39 Å for Pt, 1.24 Å for Ni) would induce a surface segregation of Pt atoms to relieve the strain.[30,31] In other words, the formation of the energetically unfavorable Pt@Ni nanoparticle in the early stage of the synthesis suggests that there is a kinetic barrier for the migration of embedded Pt atoms to the more favorable surface sites.

Figure 3a shows the relative energy of the Pt atom at each position in the cross section of a model octahedral Ni particle. Significant energy barriers (0.2−0.4 eV) exist for placing Pt atoms at the subsurface layer, consistent with previous studies,[32,33] indicating that diffusion paths to the surface are obstructed by the subsurface layer in all directions. Since the surface segregation of Pt was not observed under the Ar atmosphere (Supporting Information Figure S6), the thermal energy alone is presumably insufficient to overcome this subsurface energy barrier even under our prolonged experimental conditions, from 5 to 12 h at 170 °C. On the other hand, when CO molecules are adsorbed on the surface, as in Figure 3b, the energy barrier on the diffusion paths disappears (Figure 3d), and thus the

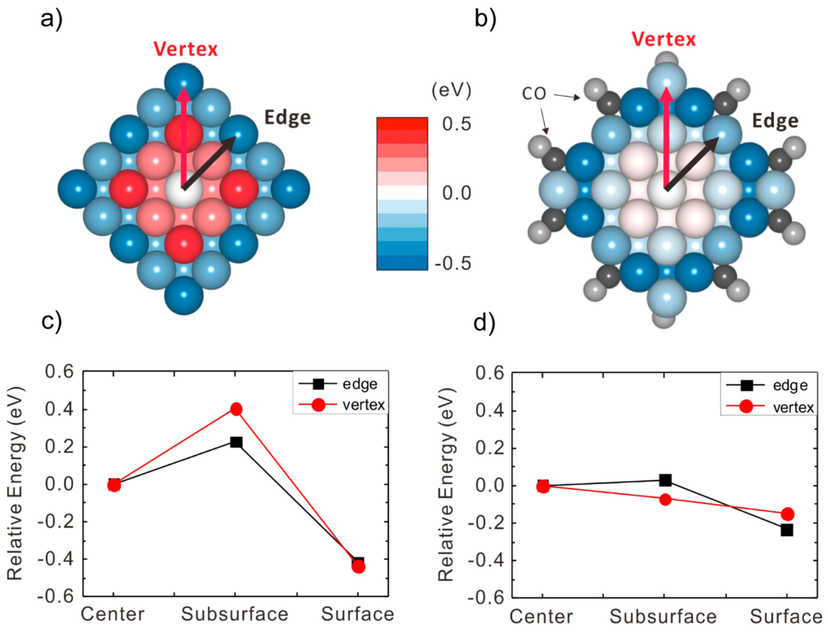

Figure 3. Relative energy of the model Ni octahedral nanoparticle when the Pt atom substitutes a Ni atom at different positions. Energy state of the nanoparticle was evaluated (a) under vacuum or (b) with CO. The energy variation along the path to either the ⟨100⟩ vertex or ⟨110⟩ edge is depicted (c) without CO and (d) with CO. For both diffusion paths, the CO adsorption on the surface reduces the energy barrier for Pt diffusion. While the diffusion to the ⟨100⟩ vertex is a thermodynamically feasible process, the energy barrier still remains on the path to the ⟨110⟩ edge direction.

embedded Pt atoms are now able to diffuse toward the outermost surface, as observed in the experiments. Strasser and co-workers also obtained the directional nanostructures by using acetylacetonate as the ligand.[25] In this case, the role of ligand was to hinder the Pt diffusion to a particular direction "by capping" due to stronger adsorption on {111} surface, while, in the present work, the CO ligand was used to facilitate the diffusion. Although the resulting directional nanostructures are similar, the mechanisms for the anisotropic segregation of the two cases are indeed different.

The instability for placing Pt atoms at the subsurface layer and its alleviation by CO adsorption can be understood from the d-band center theory, *i.e.*, by comparing the d-band center of the surface Ni atoms with and without Pt on the subsurface.[34,35] The d-band center (average of up- and down-spins) of the four Ni atoms without and with the Pt atoms on the subsurface is calculated to be −1.52 and −1.44 eV, respectively (Supporting Information Figure S7). This upward shift of the d-band center in the presence of Pt implies that to some extent the subsurface Pt destabilizes the total system by raising the electron energy of the surface Ni atoms. The d-band center theory[35] then suggests that a d-band that is closer to the Fermi level results in a stronger coupling and binding with the guest CO molecules, which eventually stabilizes the total system. To see the enhanced interfacial CO binding to the Ni surface due to the subsurface Pt atoms, we focused on the bond length variations. Indeed, when Pt locates at the subsurface layer, the distance between the surface Ni, *i.e.*, bridge sites on Ni(110), and adsorbed CO decreases from 1.848 Å to 1.840 Å (increased Ni−CO bonding), whereas the C−O bond length of adsorbed CO increases from 1.170 Å to 1.180 Å, (weakened C−O bonding).

When this subsurface migration barrier is eliminated by CO adsorption (c and d in Figure 3), the embedded Pt atoms can successfully diffuse to the surface. However, the key experimental observation was that the latter diffusion is not random, but has directionality. While the stronger interaction between CO and Pt may have some effects on the Pt migration to the surface,[36] it is likely that this surface binding effect would not extend more than a few layers. That is to say, we expect that the observed directional diffusion phenomena inside nanoparticles of 36 ± 2 nm in size would rather be governed by the internal strain energy, as described in previous studies.[30] Therefore, to model the directional diffusion, we calculated the minimum strain energy path for embedded Pt atoms diffusing through the bulk lattice. To find such a minimum energy path for Pt diffusion, we constructed the center, edge, and vertex models (Figure 4) that represent the initially embedded Pt (Figure 4a), Pt diffusion toward the ⟨110⟩ edge (Figure 4b), and Pt diffusion toward the ⟨100⟩ vertex (Figure 4c), respectively. The vertex model (−0.17 eV/Pt) is indeed noticeably lower in energy than the edge model (−0.02 eV/Pt). This result suggests that Pt atoms prefer to align along the ⟨100⟩ vertex during diffusion in the bulk of the Ni, forming the internal pillars as observed in the experiments and shown in Figure 2. While these energy differences are

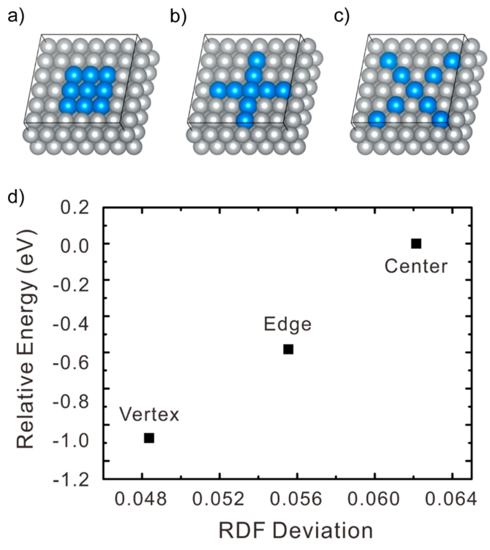

Figure 4. Relative energies of the optimized structures with different Pt arrangements in the Ni bulk model: (a) center, (b) edge, and (c) vertex. (d) Correlation between the relative stability of a particular Pt alignment and the deviation of Ni–Ni RDF (radial distribution function) from the pure Ni lattice as a measure of the extent of strain due to Pt. The strain is minimized when Pt aligns along the ⟨100⟩ vertex direction of the Ni system.

the combined net results of the Ni–Ni, Pt–Pt, and Pt–Ni interactions, the major effect may come from the Ni–Ni interaction, *i.e.*, the strain on Ni, since the Ni is the dominant component ($Pt_{0.03}Ni_{0.97}$). The lattice strain energy of Ni for each model due to the presence of Pt should be proportional to the deviation of the Ni–Ni distance from the equilibrium bond distance of pure Ni (2.487 Å). To compare the extent of deviation for both the compressive and tensile directions, we calculated the root-mean-square deviation (RMSD) of the radial distribution function (RDF) for the Ni–Ni pairs in each system. As shown in Figure 4d, the RDF deviation has a strong correlation with the relative energy of each system, which implies that the strain is indeed the key origin of the preferred Pt alignment in the interior bulk-like region of the nanoparticle.

When mapping the relative energy of placing the Pt atom on the octahedral surface sites (Supporting Information Figure S8a), the edge position is slightly energetically more favorable than the vertex position, by −0.069 eV. Therefore, the Pt atoms that were initially segregated at the ⟨100⟩ vertex due to the bulk-like diffusion would move to the surface and rearrange toward the ⟨110⟩ edge, forming the skeletal Pt–Ni structure as observed in Figure 2. Note that for Pt atoms the (111) facet is less favorable compared to the edge or vertex positions. In particular, when CO molecules are adsorbed onto the surface (Supporting Information Figure S8b), the energetically unfavorable nature of the (111) facet for Pt intensifies, which makes the Pt atoms remain on the edge. So, the combined effects of larger atom size and stronger metal–CO bond strength for Pt are expected to position the Pt atoms at the edge sites of the octahedron, resulting in the formation of thin Pt lines along the ⟨110⟩ edges of a faceted Ni nanoparticle. Remarkably, all the Pt-rich lines at the axes and edges in the nanocrystal are very uniform in thickness, and prolonged heating under CO does not completely transfer the Pt content in the axis to the surface. Therefore, it appears that once the inner axis reaches sufficient Pt phase segregation and diameter, which would stabilize the Pt-rich axes, the diffusion of Pt atoms along the grain boundary becomes very slow.

We next extended our synthetic concept to more complex, hierarchical nanostructures, which would be more beneficial in enhancing the activity and stability of nanoparticles for catalytic applications. The introduction of sodium oleate to the reaction mixture causes a drastic change in the nanoparticle growth behavior and results in the formation of a unique phase-segregated hierarchical PtNi nanostructure (PHN; $Pt_{0.06}Ni_{0.94}$, Supporting Information Figure S1) where numerous small octahedra are attached to constitute the overall structure (Figure 5a). Sodium oleate seems to interfere with the Ni shell growth on the Pt core during nanocrystal growth, plausibly by changing the nucleation and growth rate of the Ni nanocrystal. The detailed formation mechanism of PHN was studied by a temporal TEM analysis (Supporting Information Figure S9). After the formation of an imperfect Pt-based seed, the growth of small branches was observed on the tip of the seed along six different directions. This process occurs repeatedly to form a dendritic nanostructure, which eventually forms a PHN. Again, CO-binding induces the Pt segregation along the nanostructure growth directions, which is clearly seen along the edges of all the constituting small octahedrons by the HAADF-STEM image (Figure 5a). The segregated Pt phase on the edges of the PON (Figure 1a) and the PHN can provide further growth sites for other nanoparticles. Reaction with the Au precursor led to the growth of Au nanoparticles on both the vertices and edges (Supporting Information Figure S10). In this case, a slight preference for vertex growth was observed, indicating the highly reactive nature of the nanoparticle vertices. The unobserved growth of Au on the Ni-rich facet can be explained by considering both the lattice parameter differences and the stable CO-stabilized Ni{111} facets.

Nanoframe structures of catalytic metals are receiving a great deal of interest due to their atom efficiency in catalysis;[16] these structures have high atom efficiency because catalytic activity is directly related to the exposed surface area.[14,15] The Ni component in the PON ($Pt_{0.03}Ni_{0.97}$) and PHN ($Pt_{0.06}Ni_{0.94}$) could be conveniently removed by treating with acetic acid to give an octahedral skeletal Pt-based nanostructure (OSN; $Pt_{0.70}Ni_{0.30}$, Figure 5b) with three orthogonal axes and a

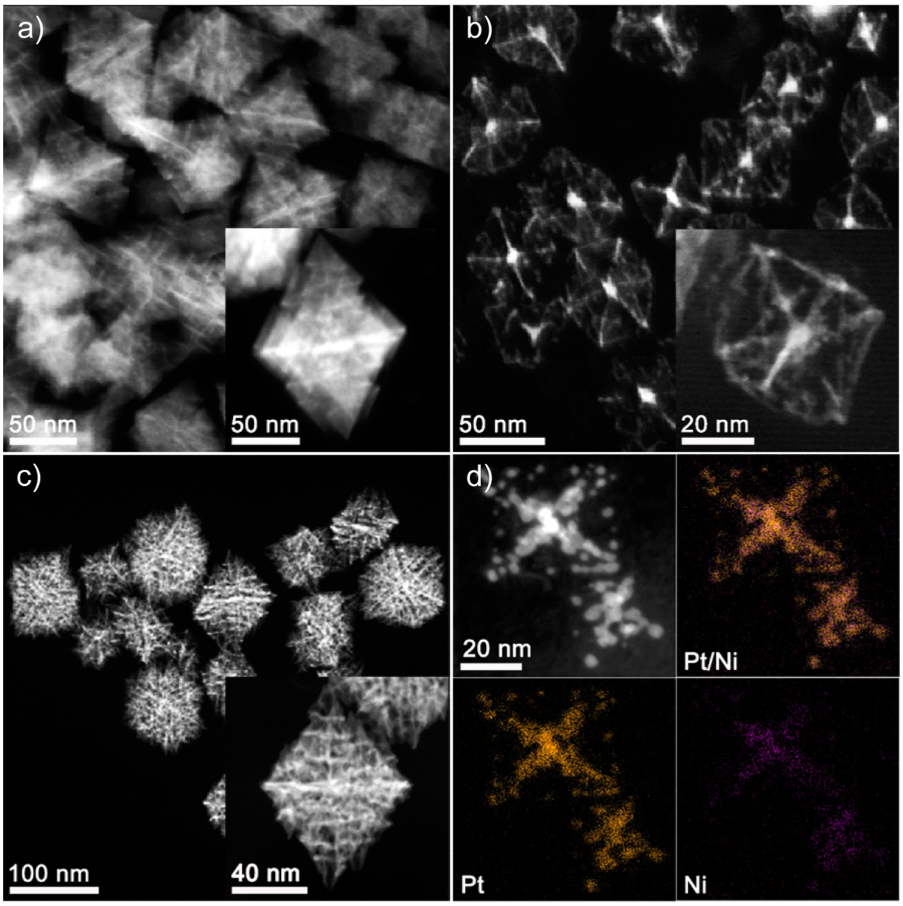

Figure 5. HAADF-STEM and EDS elemental mapping images of phase-segregated nanoparticles. HAADF-STEM images of (a) PHN, (b) OSN, and (c) HSN. OSN and HSN structures made with PON and PHN by a chemical etching process. (d) EDS elemental mapping of OSN, which demonstrates the dominant Pt (orange) component in the axes and edges of the nanostructure, with the distribution of a small amount of the Ni (purple) component.

hierarchical skeletal Pt-based nanostructure (HSN; $Pt_{0.82}Ni_{0.18}$, Figure 5c), respectively (Supporting Information Figure S1). As shown in Figure 5d and Supporting Information Figure S1, EDS elemental mapping and quantitative analysis of the Pt-rich nanoframeworks show the presence of some remnant Ni content in the structures, and therefore the framework nanostructures are best described as PtNi alloys, likely Pt/Ni solid solutions, with Pt as the dominant phase. The dominant X-ray diffraction (XRD) peaks of PON and PHN of (111) Ni are not observed in XRD patterns of OSN and HSN, where only $Pt_{0.70}Ni_{0.30}$ and $Pt_{0.82}Ni_{0.18}$ alloy, likely Pt/Ni solid solution, phases are present after Ni removal (Supporting Information Figure S11). The differences in the Ni-doping between OSN and HSN result from the differences in the initial Ni/Pt precursor ratios as well as the differences in the reaction conditions. On the other hand, the OSN obtained by acid etching of the phase-segregated Ni-rich part provides further growth sites for small Pt nanocrystallites, leading to a nanoframe structure with an overgrown Pt phase (OSN_OV; $Pt_{0.87}Ni_{0.13}$) (Supporting Information Figure S12). The HSN can be treated similarly to form hierarchical skeletal Pt-based nanoparticles with an overgrown Pt phase (HSN_OV; $Pt_{0.86}Ni_{0.14}$) (Supporting Information Figure S12). Indiscriminate Pt growth on the edges and vertices of skeletal Pt nanostructures seems to indicate the remarkable reactivity of the skeletal Pt nanostructures (detailed TEM analysis results of the prepared nanostructures are shown in Supporting Information Figures S13−S15). A number of methodologies have been developed to prepare nanoframework strcutures or a phase segregation system, and the atom replacement or deposition on the template nanoparticle surface is usually required for their formation.[16,18,25,37−39] The nanoframework formation of this study differs greatly from the previous works in that the framework structure formation can occur even in the nanoparticle matrix, not confined to the surface only.

By taking advantage of the highly reactive nature and open hollow structure of the skeletal Pt-based nanostructures, we investigated the electrocatalytic performances of the OSN and HSN for ORR by rotating disk electrode measurements (Figure 6). To assess the ORR activity of the skeletal Pt-based nanostructures, the carbon black supported catalysts (OSN/C and HSN/C) were prepared (Supporting Information Figure S16). The electrochemically active surface areas of the catalysts

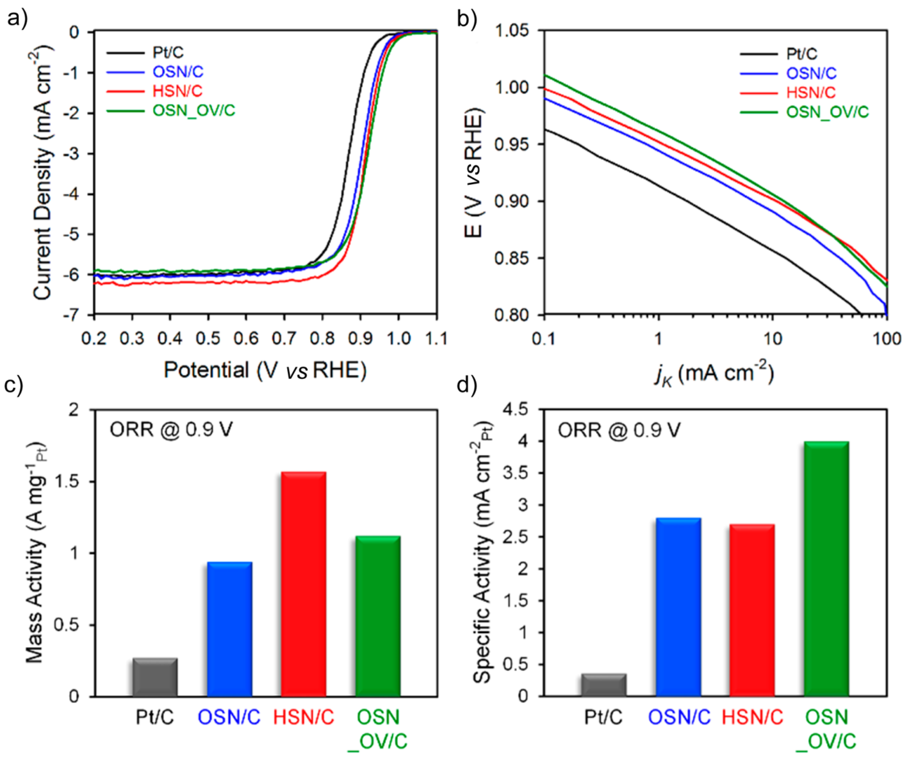

Figure 6. Electrochemical characterization of PtNi catalysts. (a) Linear sweep voltammetry curves of Pt/C, OSN/C, HSN/C, and OSN_OV/C and (b) their corresponding Tafel plots for the ORR in an O_2-saturated 0.1 M $HClO_4$ solution (1600 rpm, 20 mV s^{-1}). The Pt loading on the electrode is 7.2 μg cm^{-2} for OSN/C and HSN/C, 11.2 μg cm^{-2} for OSN_OV/C, and 6.7 μg cm^{-2} for Pt/C. (c) Mass activities and (d) specific activities of Pt/C OSN/C, HSN/C, and OSN OV/C at 0.9 V *vs* RHE.

TABLE 2. Electrocatalytic Activity of the Catalysts

	half-wave potential (V *vs* RHE)[a]	ECSA (m^2 g^{-1})[b]	MA @ 0.9 V (A mg_{Pt}^{-1})[c]	SA @ 0.9 V (mA cm_{Pt}^{-2})[d]
commercial Pt/C	0.87	69	0.27	0.36
OSN/C	0.905	34	0.94 (×3.5)[e]	2.8 (×7.8)[e]
HSN/C	0.915	58	1.57 (×5.8)[e]	2.7 (×7.5)[e]
OSN_OV/C	0.92	28	1.12 (×4.1)[e]	4.0 (×11.1)[e]

[a] Half-wave potential obtained at which the measured current is equal to one-half of the diffusion-limited current value. [b] Electrochemically active surface area (ECSA) calculated from cyclic voltammetry curves. [c] Mass activity (MA) estimated from kinetic current at 0.9 V normalized to the Pt loading of the disk electrode. [d] Specific activity (SA) estimated from kinetic current at 0.9 V normalized to the ECSA of the catalyst. [e] Numbers in parentheses indicate an improvement factor *versus* commercial Pt/C catalyst.

were obtained by cyclic voltammetry (Supporting Information Figure S17), and their ORR activity was evaluated by linear sweep voltammetry (LSV) in O_2-saturated 0.1 M $HClO_4$ solution, at a scan rate of 20 mV s^{-1} and a rotating speed of 1600 rpm. The LSV curves (Figure 6a) and mass-transport-corrected kinetic currents (Figure 6b) clearly demonstrated the enhancement in ORR activity in the skeletal Pt nanostructure catalysts when compared to the commercial Pt/C catalyst (Johnson-Matthey, HiSPEC 2000). The OSN/C catalyst showed a positively shifted half-wave potential (0.905 V) compared to that of Pt/C (0.87 V), and a further shift was observed with the HSN/C catalyst (0.915 V). As shown in Figure 6c, the mass activities of OSN/C and HSN/C catalysts were 0.94 and 1.57 A mg_{Pt}^{-1} at 0.9 V, which were higher than that of the Pt/C catalyst (0.27 A mg_{Pt}^{-1}) by a factor of 3.5 and 5.8, respectively. These mass activities are higher than the U.S. Department of Energy's 2017 target (0.44 A mg_{Pt}^{-1}) and represent one of the best activities among the recently reported Pt–Ni-based catalysts.[4–16] The specific activities of the catalysts (Figure 6d) were calculated to be 2.8 and 2.7 mA cm_{Pt}^{-2} at 0.9 V *vs* RHE (reversible hydrogen electrode), which were 7.8 and 7.5 times higher than that from the Pt/C catalyst (0.36 mA cm_{Pt}^{-2}). The detailed electrochemical properties are summarized in Table 2.

The enhancement in the ORR activity observed in the Pt skeletal nanostructure catalysts can be attributed to electronic effects as well as their skeletal morphologies. In Pt skeletal nanostructures, remnant Ni atoms occupy subsurface layers under the outermost Pt layer, due to preferential Pt–CO binding. It was reported that the electronic structure of Pt skin atoms could be altered by subsurface Ni layers, causing a lower surface coverage of spectator oxygenated species (OH_{ad}) and hence superior catalytic properties.[14] Notably, we could generate such a desirable "Pt skin on Pt−Ni alloy (likely Pt/Ni solid solution)" structure in a simple manner by CO-induced spontaneous phase segregation, instead of using the previously employed thermal annealing process.[16] The 3D cage-like geometry of the skeletal Pt nanostructure can also contribute to the enhanced ORR performance, as the nanoconfinement effect in such structures can lead to increased attempt frequencies and improved kinetics for the ORR.[7] It should be noted that the higher ORR activity of the HSN/C catalyst compared to that of the OSN/C catalyst can be attributed to its highly integrated structure; the hierarchical structure of the HSN/C catalyst causes increased collision frequency of the reactive species, which enhances the probability of a reactant molecule undergoing an electron transfer, leading to an enhancement in electrochemical kinetics. To further exploit the morphological enhancement effect, we examined the ORR activity of OSN_OV, where a secondary Pt structure was grown over the OSN, and measured its ORR activity. As shown Figure 6, the OSN_OV/C catalyst clearly showed much higher ORR activity as compared to that of the OSN/C catalyst, evidenced by a positively shifted half-wave potential (0.920 V) and mass and specific activities, which support the possible nanoconfinement effect.

We also investigated the electrochemical stability of the HSN/C catalyst by cycling 10 000 times between 0.6 and 1.0 V at a scan rate of 50 mV s^{-1}. After the cycling, the LSV of the HSN/C catalyst showed a negative shift of only 20 mV, indicating its high stability (Supporting Information Figure S18b). As explained above, the enhanced durability could be ascribed to the electronic structure of the Pt skin surface resulting in a lower coverage of oxygenated intermediates because of the weaker oxygen binding strength, which diminishes the probability of Pt dissolution.[14] Also, the electron transfer numbers of all catalysts are nearly four, strongly suggesting that the ORR on these four catalysts proceeds *via* a direct four-electron process (Supporting Information Figure S19).

CONCLUSIONS

We have demonstrated the feasibility of three-dimensional alloy composition control within a faceted nanocrystal by utilizing the energy gradients induced by surface-bound moieties and offered theoretical explanations. The formation of visually identifiable, well-defined atom diffusion passages would provide a powerful synthetic tool for the design of unconventional three-dimensional nanostructures. We also showed that selective dealloying of the nanocrystals with geometrically precise phase segregation can result in highly active skeletal nanocatalysts. We believe that postsynthetic nanoscale structural engineering for regiospecific alloy composition control would open up new avenues for drastic improvements in catalytic activity by enabling hitherto unapproachable complex nanostructure designs.

METHODS SECTION

Reagents. $Pt(acac)_2$ (97%), $Ni(acac)_2$ (95%), $HAuCl_4$ (99.99%), K_2PtCl_4 (98%), stearic acid (95%), octadecylamine (90%), oleylamine (70%), ethylene glycol (99.8%), and acetic acid (99.7%) were purchased from Sigma-Aldrich. Sodium oleate (97%) was purchased from Tokyo Chemical Industry Co. Ltd. All reagents were used as received without further purification.

Material Characterization. TEM and HRTEM studies were carried out in a Tecnai G2 F30ST microscope and Tecnai G2 20 S-twin microscope. Aberration-corrected imaging and high spatial resolution EDS were performed at FEI Nanoport in Eindhoven using a Titan Probe Cs TEM 300 kV with Chemi-STEM technology. EDS elemental mapping data were collected using a higher efficiency detection system (Super-X detector with XFEG); it integrates four FEI-designed silicon drift detectors very close to the sample area. Compared to a conventional EDX detector with Schottky FEG systems, ChemiSTEM produces up to 5 times the X-ray generation with the X-FEG and up to 10 times the X-ray collection with the Super-X detector. X-ray diffraction patterns were collected to understand the crystal structures of PtNi nanocrystals with a Rigaku Ultima III diffractometer system using graphite-monochromatized Cu Kα radiation at 40 kV and 30 mA.

Phase-Segregated Octahedral PtNi Nanoparticle. A slurry of $Pt(acac)_2$ (0.06 mmol), $Ni(acac)_2$ (0.72 mmol), stearic acid (0.35 mmol), and octadecylamine (15 mmol) was prepared in a 100 mL Schlenk tube, equipped with a magnetic stirrer. The slurry was evacuated for 5 min in an oil bath preheated to 80 °C, and then the reaction mixture under CO gas (flow rate = 20 cm^3/min) was placed in an oil bath preheated to 170 °C, equipped with a bubbler. After 3 min, CO gas injection to the Schlenk tube was stopped, and the solution was kept at 170 °C for 5 h under 1 atm of CO gas. The product was cooled to room temperature and then centrifuged with added ethanol/toluene (v/v = 20 mL/15 mL) to form a black precipitate.

Core−Shell Pt@Ni Concave Nanocube. A slurry of $Pt(acac)_2$ (0.06 mmol), $Ni(acac)_2$ (0.72 mmol), stearic acid (0.35 mmol), and octadecylamine (15 mmol) was prepared in a 100 mL Schlenk tube, equipped with a magnetic stirrer. The slurry was evacuated for 5 min in an oil bath preheated to 80 °C, and then the reaction mixture under CO gas (flow rate = 20 cm^3/min) was placed in an oil bath preheated to 170 °C, equipped with a bubbler. After 3 min, CO gas injection to the Schlenk tube was stopped, and the solution was kept at 170 °C under 1 atm of CO gas. After 1 h, the Schlenk tube was evacuated for 45 min (**Caution:** *Proceed with an extreme care!*), and the solution was kept at 170 °C for 12 h under Ar gas (flow rate = 10 cm^3/min). The product was cooled to room temperature and then centrifuged with added ethanol/toluene (v/v = 20 mL/15 mL) to form a black precipitate.

Phase-Segregated Hierarchical PtNi Nanoparticle. A slurry of $Pt(acac)_2$ (0.06 mmol), $Ni(acac)_2$ (0.72 mmol), stearic acid (0.35 mmol), sodium oleate (0.35 mmol), and octadecylamine (15 mmol) was prepared in a 100 mL Schlenk tube, equipped with a magnetic stirrer. The slurry was evacuated for 5 min in an oil bath preheated to 80 °C, and then the reaction mixture under CO gas (flow rate = 20 cm^3/min) was placed in an oil bath preheated to 200 °C, equipped with a bubbler. After 3 min, CO gas injection to the Schlenk tube was stopped, and the solution was kept at 200 °C for 5 h under 1 atm of CO gas. The product was cooled to room temperature and then centrifuged with added deionized water (18.2 MΩ·cm, Millipore)/*n*-propanol/methanol (v/v/v = 15 mL/10 mL/15 mL) to form a black precipitate. The black precipitate was further washed with ethanol/toluene (v/v = 20 mL/15 mL).

Au Overgrowth on Phase-Segregated Octahedral PtNi Nanoparticle. A slurry of PONs (50 mg) and octadecylamine (10 mmol) was prepared in a 100 mL Schlenk tube, equipped with a bubbler and a magnetic stirrer. The reaction mixture under Ar gas (flow rate = 10 cm^3/min) was placed in an oil bath preheated to 110 °C. After 5 min, a solution of $HAuCl_4$ (25 mg) in oleylamine (1 mL) was injected into the reaction mixture. The reaction mixture was kept at 110 °C for 1 h under Ar gas. The product was cooled to room temperature and then centrifuged with added ethanol/toluene (v/v = 20 mL/15 mL) to form a black-purple precipitate.

Au Overgrowth on Phase-Segregated Hierarchical PtNi Nanoparticle. A slurry of PHNs (50 mg) and octadecylamine (10 mmol) was prepared in a 100 mL Schlenk tube, equipped with a bubbler and a magnetic stirrer. The reaction mixture under Ar gas (flow rate = 10 cm^3/min) was placed in an oil bath preheated to 110 °C. After 5 min, a solution of $HAuCl_4$ (50 mg) in oleylamine (2 mL) was injected into the reaction mixture. The solution was kept at 110 °C for 1 h under Ar gas. The product was cooled to room temperature and then centrifuged with added ethanol/toluene (v/v = 20 mL/15 mL) to form a black-purple precipitate.

Octahedral Skeletal Pt-Based Nanoparticle . The OSN was made from a PON by etching the Ni component by acetic acid. Typically, a slurry of PONs (from 50 to 100 mg) and acetic acid (10 mL) was prepared in a 100 mL Schlenk tube, equipped with a magnetic stirrer. The reaction mixture was heated for 1 h under air in an oil bath preheated to 100 °C. The product was cooled to room temperature and then centrifuged with added ethanol to form a black precipitate.

Hierarchical Skeletal Pt-Based Nanoparticle. The HSN was made from a PHN by etching the Ni component by acetic acid. Typically, a slurry of PHNs (from 50 to 100 mg) and acetic acid (20 mL) was prepared in a 100 mL Schlenk tube, equipped with a magnetic stirrer. The reaction mixture was heated for 1 h under air in an oil bath preheated to 100 °C. The product was cooled to room temperature and then centrifuged with added ethanol to form a black precipitate.

Pt Overgrowth on Octahedral Skeletal Pt-Based Nanoparticle. The OSN_OV was made from a PON by etching the Ni component of the PON and growing Pt simultaneously. Typically, a slurry of PONs (50 mg), acetic acid (5 mL), and ethylene glycol (1 mL) was prepared in a 100 mL Schlenk tube, equipped with a bubbler and a magnetic stirrer. The reaction mixture under Ar gas (flow rate = 10 cm^3/min) was placed in an oil bath preheated to 90 °C. After 1 min, a solution of K_2PtCl_4 (25 mg) in deionized water (18.2 MΩ·cm, Millipore, 1 mL) was injected into the reaction mixture. The solution was kept at 90 °C for 5 h under Ar gas. The product was cooled to room temperature and then centrifuged with added ethanol to form a black precipitate.

Pt Overgrowth on Hierarchical Skeletal Pt-Based Nanoparticle. The HSN_OV was made from a PHN by etching the Ni component of PHN and growing Pt simultaneously. Typically, a slurry of PHN (50 mg), acetic acid (10 mL), and ethylene glycol (1 mL) was prepared in a 100 mL Schlenk tube, equipped with a bubbler and a magnetic stirrer. The reaction mixture under Ar gas (flow rate = 10 cm^3/min) was placed in an oil bath preheated to 90 °C. After 1 min, a solution of K_2PtCl_4 (50 mg) in deionized water (18.2 MΩ·cm, Millipore, 1 mL) was injected into the reaction mixture. The solution was kept at 90 °C for 5 h under Ar gas. The product was cooled to room temperature and then centrifuged with added ethanol to form a black precipitate.

Carbon-Supported Octahedral Skeletal Pt-Based Nanoparticle Catalyst and Hierarchical Skeletal Pt-Based Nanoparticle Catalyst. The OSN/C was produced by preparing the carbon-supported PON (PON/C) and then etching the Ni component of the PON/C by acetic acid. The PON (1 mg) was dispersed in chloroform (1 mL), and the slurry was sonicated for 1 h. In a separate vessel, carbon black (Vulcan XC-72, Cabot, 1 mg) was dispersed in chloroform (1 mL) and sonicated for 1 h. The PON slurry was added dropwise to the carbon-containing slurry, and the mixture was sonicated further for 1 h. The black precipitate, PON/C, was obtained by washing several times with ethanol, and the product was dried by flowing Ar gas. In order to etch the Ni component from the PON/C, the sample was dispersed in 100 mL of acetic acid and heated at 70 °C for 10 h under magnetic stirring. After filtration, the precipitate was washed several times with ethanol and dried overnight by flowing Ar gas. The preparation of the HSN/C catalyst was carried out by the same procedure as described for the OSN/C catalyst by using PHNs instead of PONs.

Carbon-Supported Pt Overgrown Octahedral Skeletal Pt-Based Nanoparticle Catalyst. A slurry of OSN_OV (10 mg) in chloroform (10 mL) was mixed with oleylamine (1 mL), and the solution was sonicated for 1 h. In a separate vessel, carbon black (Vulcan XC-72, Cabot, 40 mg) was dispersed in chloroform (40 mL) and sonicated for 1 h. The OSN_OV dispersion was added dropwise to the carbon-containing slurry, and the mixture was sonicated further for 1 h. A black precipitate was obtained by washing several times with ethanol.

Electrochemical Measurements. Electrochemical characterization of samples was carried out using an IviumStat electrochemical analyzer. The electrochemical experiments were performed at room temperature (25 °C) under atmospheric pressure using a three-compartment electrochemical cell. A graphite counter electrode and hydrogen reference electrode (Hydroflex, Gaskatel) were used. All potentials in this study are referenced to the reversible hydrogen electrode. For the oxygen reduction reaction performance measurement, a rotating disk electrode (RDE, ALS) with a glassy carbon disk (GC, 4 mm in diameter) was used as the working electrode (ALS, Cat. No. 012613). The RDE was polished with 1.0 and 0.3 μm alumina suspensions to generate a mirror finish. The catalyst ink was prepared by mixing the catalyst (5 mg), 5 wt % Nafion (40 μL, Aldrich), deionized water (100 μL), and ethanol (1.06 mL, >99.9%, Samchun) using ultrasonication for at least 30 min. A 2.0 μL amount of the ink was dropped and dried to form a thin film on a glassy carbon disk electrode with a 0.126 cm^2 geometric surface area. Prior to the electrochemical measurements, a potential cycle from 0.05 to 1.2 V was applied in a N_2-saturated solution of 0.1 M $HClO_4$ for 20 cycles at a scan rate of 100 mV s^{-1} for electrochemical cleaning. The cyclic voltammogram was obtained under the same conditions used for electrochemical cleaning, except the scan rate was changed to 50 mV s^{-1} for 3 cycles. Linear sweep voltammetry curves for the ORR were obtained using a potential cycle from 0.2 to 1.1 V in an O_2-saturated solution of 0.1 M $HClO_4$ with O_2 purging at a rotation speed of 1600 rpm and a scan rate of 20 mV s^{-1}. Currents were collected after *iR*-drop correction. An electrochemical stability test was conducted in N_2-saturated 0.1 M $HClO_4$ solution in the potential range from 0.6 to 1.0 V *vs* RHE at a scan rate of 50 mV s^{-1} for 10 000 cycles. After the cycling, the ORR activity was obtained in a fresh electrolyte. The ORR polarization curves before and after potential cycling were obtained under the same conditions used for the above ORR measurement.

Theoretical Calculations. In order to investigate the diffusion of Pt atoms in the Ni octahedral nanoparticle system, spin-polarized DFT calculations were performed using the Vienna ab initio simulation package (VASP).[40] The Perdew–Burke–Ernzerhof (PBE) exchange–correlation functional[41] and projector-augmented wave (PAW) method,[42] along with a plane wave energy cutoff of 400 eV, were used. For the k-point mesh, the single gamma point calculation was performed for the 85-atom nanoparticle model, and for the bulk system 2 × 2 × 4 Monkhorst–Pack k-points mesh sampling was used.

To study the diffusion of Pt atoms in the Pt–Ni octahedral nanoparticle, the total energies of the model nanoparticles having one Pt atom in different positions were compared (Supporting Information Figure S20b). The reference position of the Pt atom would be the center of the Ni octahedral nanoparticle. Among the 85 Ni atoms of the octahedral nanoparticle, one Pt atom would substitute for the Ni and the total energy would be compared to the one with Pt at the reference position.

For this specific octahedral nanoparticle to mimic the experimental CO-rich condition, 32 CO molecules were attached to the lowest energy sites on the nanoparticle surface. The CO coverage was set to 0.5, where the sticking probability and the adsorption heat of CO on the Ni surface start to decrease.[43] Since the edges of the nanoparticle are more exposed and generally thermodynamically less stable, the CO molecule would be adsorbed to the edge first and then the remaining sites on the (111) surface.[44] Because the Ni atoms on the edge can be considered as the (110) surface, the CO molecules were placed on the bridge sites that are the most stable adsorption sites on the (110) surface.[45,46] To maintain the symmetry and the distance between the CO molecules, a CO molecule was placed on each of the remaining hollow sites that would be the most stable sites on the (111) surface.[47] As a result, 24 CO molecules were adsorbed on the edge and eight CO molecules were adsorbed on the surface of the octahedral nanoparticle.

To understand the mechanism of Pt diffusion in the experimental nanoparticles of size 36.5 ± 2 nm, we essentially considered the bulk lattice since the surface and confinement effects can be expected to propagate not much further than the first four metal atom layers.[30,45,48] Therefore, the pure Ni supercell was constructed with 144 Ni atoms to represent the innermost portion of the Ni nanoparticles where the diffusion of core metals is initiated. On the center layer in the supercell, nine Ni atoms were substituted with Pt atoms to replicate three different states of Pt diffusion in the Ni nanoparticle. The Pt atoms were assembled together in the center to demonstrate the initial state before the Pt diffusion was activated (Figure 4a). To simulate the diffusion to the edge (Figure 4b) and the vertex (Figure 4c), the nine Pt atoms were arranged to have the same direction as if they were diffusing inside the octahedral nanoparticle.

Conflict of Interest: The authors declare no competing financial interest.

Supporting Information Available: Additional material characterization and analysis. This material is available free of charge *via* the Internet at http://pubs.acs.org.

Acknowledgment. K.L. and A.O. conceived and designed the research. K.L., Y.J., and S.H.J. supervised the research and co-wrote the manuscript. A.O. performed the chemical synthetic work, material characterization, and analysis of the data. H.B. performed the TEM analysis. D.S.C. and H.K. performed theoretical calculations and data analysis. J.Y.C. and S.K. carried out electrochemical measurements and data analysis. B.K. analyzed data, drew the illustrations, and aggregated the figures. All authors discussed the results and commented on the manuscript. This work was supported by National Research Foundation of Korea grants (NRF-2013R1A2A2A01015168, NRF-20100020209, NRF-2014R1A4A1003712, and NRF-2013R1A1A2012960) funded by the Korea government (MSIP). This work was also supported by IBS-R023-D1-2015-a00. The authors thank Korea Basic Science Institute (KBSI) for the usage of their HRTEM instrument.

REFERENCES AND NOTES

1. Guo, S.; Zhang, S.; Sun, S. Tuning Nanoparticle Catalysis for the Oxygen Reduction Reaction. *Angew. Chem., Int. Ed.* **2013**, *52*, 8526–8544.
2. Xia, Y.; Xiong, Y.; Lim, B.; Skrabalak, S. E. Shape-Controlled Synthesis of Metal Nanocrystals: Simple Chemistry Meets Complex Physics. *Angew. Chem., Int. Ed.* **2009**, *48*, 60–103.
3. Habas, S. E.; Lee, H.; Radmilovic, V.; Somorjai, G. A.; Yang, P. Shaping Binary Metal Nanocrystals through Epitaxial Seeded Growth. *Nat. Mater.* **2007**, *6*, 692–697.
4. Gan, L.; Heggen, M.; Rudi, S.; Strasser, P. Core−Shell Compositional Fine Structures of Dealloyed Pt_xNi_{1-x} Nanoparticles and Their Impact on Oxygen Reduction Catalysis. *Nano Lett.* **2012**, *12*, 5423–5430.
5. Kuttiyiel, K. A.; Sasaki, K.; Choi, Y. M.; Su, D.; Liu, P.; Adzic, R. R. Nitride Stabilized PtNi Core−Shell Nanocatalyst for High Oxygen Reduction Activity. *Nano Lett.* **2012**, *12*, 6266–6271.
6. Carpenter, M. K.; Moylan, T. E.; Kukreja, R. S.; Atwan, M. H.; Tessema, M. M. Solvothermal Synthesis of Platinum Alloy Nanoparticles for Oxygen Reduction Electrocatalysis. *J. Am. Chem. Soc.* **2012**, *134*, 8535–8542.
7. Snyder, J.; McCue, I.; Livi, K.; Erlebacher, J. Structure/Processing/Properties Relationships in Nanoporous Nanoparticles as Applied to Catalysis of the Cathodic Oxygen Reduction Reaction. *J. Am. Chem. Soc.* **2012**, *134*, 8633–8645.
8. Wu, J.; Qi, L.; You, H.; Gross, A.; Li, J.; Yang, H. Icosahedral Platinum Alloy Nanocrystals with Enhanced Electrocatalytic Activities. *J. Am. Chem. Soc.* **2012**, *134*, 11880–11883.
9. Wang, D.; Xin, H. L.; Hovden, R.; Wang, H.; Yu, Y.; Muller, D. A.; DiSalvo, F. J.; Abruña, H. D. Structurally Ordered Intermetallic Platinum−Cobalt Core−Shell Nanoparticles with Enhanced Activity and Stability as Oxygen Reduction Electrocatalysts. *Nat. Mater.* **2013**, *12*, 81–87.
10. Huang, X.; Zhu, E.; Chen, Y.; Li, Y.; Chiu, C. Y.; Xu, Y.; Lin, Z.; Duan, X.; Huang, Y. A Facile Strategy to Pt_3Ni Nanocrystals with Highly Porous Features as an Enhanced Oxygen Reduction Reaction Catalyst. *Adv. Mater.* **2013**, *25*, 2974–2979.
11. Choi, S. I.; Xie, S.; Shao, M.; Odell, J. H.; Lu, N.; Peng, H. C.; Protsailo, L.; Guerrero, S.; Park, J.; Xia, X.; *et al.* Synthesis and Characterization of 9 nm Pt−Ni Octahedra with a Record High Activity of 3.3 A/mg_{Pt} for the Oxygen Reduction Reaction. *Nano Lett.* **2013**, *13*, 3420–3425.
12. Greeley, J.; Mavrikakis, M. Alloy Catalysts Designed from First Principles. *Nat. Mater.* **2004**, *3*, 810–815.
13. Stamenkovic, V. R.; Mun, B. S.; Arenz, M.; Mayrhofer, K. J. J.; Lucas, C. A.; Wang, G.; Ross, P. N.; Markovic, N. M. Trends in Electrocatalysis on Extended and Nanoscale Pt−Bimetallic Alloy Surfaces. *Nat. Mater.* **2007**, *6*, 241–247.
14. Stamenkovic, V. R.; Fowler, B.; Mun, B. S.; Wang, G.; Ross, P. N.; Lucas, C. A.; Marković, N. M. Improved Oxygen Reduction Activity on $Pt_3Ni(111)$ *via* Increased Surface Site Availability. *Science* **2007**, *315*, 493–497.
15. Cui, C.; Gan, L.; Heggen, M.; Rudi, S.; Strasser, P. Compositional Segregation in Shaped Pt Alloy Nanoparticles and Their Structural Behavior during Electrocatalysis. *Nat. Mater.* **2013**, *12*, 765–771.
16. Chen, C.; Kang, Y.; Huo, Z.; Zhu, Z.; Huang, W.; Xin, H. L.; Snyder, J. D.; Li, D.; Herron, J. A.; Mavrikakis, M.; *et al.* Highly Crystalline Multimetallic Nanoframes with Three-Dimensional Electrocatalytic Surfaces. *Science* **2014**, *343*, 1339–1343.
17. Cui, C. H.; Li, H. H.; Liu, X. J.; Gao, M. R.; Yu, S. H. Surface Composition and Lattice Ordering−Controlled Activity and Durability of CuPt Electrocatalysts for Oxygen Reduction Reaction. *ACS Catal.* **2012**, *2*, 916–924.
18. Wu, Y.; Wang, D.; Zhou, G.; Yu, R.; Chen, C.; Li, Y. Sophisticated Construction of Au Islands on Pt−Ni: An Ideal Trimetallic Nanoframe Catalyst. *J. Am. Chem. Soc.* **2014**, *136*, 11594–11597.
19. Ahmadi, M.; Behafarid, F.; Cui, C.; Strasser, P.; Cuenya, B. R. Long-Range Segregation Phenomena in Shape-Selected Bimetallic Nanoparticles: Chemical State Effects. *ACS Nano* **2013**, *7*, 9195–9204.
20. Tao, F.; Grass, M. E.; Zhang, Y.; Butcher, D. R.; Renzas, J. R.; Liu, Z.; Chung, J. Y.; Mun, B. S.; Salmeron, M.; Somorjai, G. A. Reaction-Driven Restructuring of Rh−Pd and Pt−Pd Core−Shell Nanoparticles. *Science* **2008**, *322*, 932–934.
21. Hardeveld, R. V.; Hartog, F. The Statistics of Surface Atoms and Surface Sites on Metal Crystals. *Surf. Sci.* **1969**, *15*, 189–230.
22. Ruban, A. V.; Skriver, H. L.; Nørskov, J. K. Surface Segregation Energies in Transition-Metal Alloys. *Phys. Rev. B* **1999**, *59*, 15990–16000.
23. Deng, L.; Hu, W.; Deng, H.; Xiao, S.; Tang, J. Au−Ag Bimetallic Nanoparticles: Surface Segregation and Atomic-Scale Structure. *J. Phys. Chem. C* **2011**, *115*, 11355–11363.
24. Yin, Y.; Rioux, R. M.; Erdonmez, C. K.; Hughes, S.; Somorjai, G. A.; Alivisatos, A. P. Formation of Hollow Nanocrystals through the Nanoscale Kirkendall Effect. *Science* **2004**, *304*, 711–714.
25. Gan, L.; Cui, C.; Heggen, M.; Dionigi, F.; Rudi, S.; Strasser, P. Element-Specific Anisotropic Growth of Shaped Platinum Alloy Nanocrystals. *Science* **2014**, *346*, 1502–1506.
26. Wu, J.; Gross, A.; Yang, H. Shape and Composition-Controlled Platinum Alloy Nanocrystals Using Carbon

Monoxide as Reducing Agent. *Nano Lett.* **2011**, *11*, 798–802.
27. Abild-Pedersen, F.; Andersson, M. P. CO Adsorption Energies on Metals with Correction for High Coordination Adsorption Sites — A Density Functional Study. *Surf. Sci.* **2007**, *601*, 1747–1753.
28. Zhang, J.; Yang, H.; Fang, J.; Zou, S. Synthesis and Oxygen Reduction Activity of Shape-Controlled Pt_3Ni Nanopolyhedra. *Nano Lett.* **2010**, *10*, 638–644.
29. Mayrhofer, K. J. J.; Juhart, V.; Hartl, K.; Hanzlik, M.; Arenz, M. Adsorbate-Induced Surface Segregation for Core−Shell Nanocatalysts. *Angew. Chem., Int. Ed.* **2009**, *48*, 3529–3531.
30. Wang, G.; Van Hove, M. A.; Ross, P. N.; Baskes, M. I. Quantitative Prediction of Surface Segregation in Bimetallic Pt−M Alloy Nanoparticles (M = Ni, Re, Mo). *Prog. Surf. Sci.* **2005**, *79*, 28–45.
31. Cui, C.; Ahmadi, M.; Behafarid, F.; Gan, L.; Neumann, M.; Heggen, M.; Cuenya, B. R.; Strasser, P. Shape-Selected Bimetallic Nanoparticle Electrocatalysts: Evolution of Their Atomic-Scale Structure, Chemical Composition, and Electrochemical Reactivity under Various Chemical Environments. *Faraday Discuss.* **2013**, *162*, 91–112.
32. Wang, G.; Van Hove, M. A.; Ross, P. N.; Baskes, M. I. Monte Carlo Simulations of Segregation in Pt−Ni Catalyst Nanoparticles. *J. Chem. Phys.* **2005**, *122*, 024706.
33. Ma, Y.; Balbuena, P. B. Pt Surface Segregation in Bimetallic Pt_3M Alloys: A Density Functional Theory Study. *Surf. Sci.* **2008**, *602*, 107–113.
34. Greeley, J.; Nørskov, J. K.; Mavrikakis, M. Electronic Structure and Catalysis on Metal Surfaces. *Annu. Rev. Phys. Chem.* **2002**, *53*, 319–348.
35. Nørskov, J. K.; Abild-Pedersen, F.; Studt, F.; Bligaard, T. Density Functional Theory in Surface Chemistry and Catalysis. *Proc. Natl. Acad. Sci. U.S.A.* **2011**, *108*, 937–943.
36. Zeinalipour-Yazdi, C. D.; Cooksy, A. L.; Efstathiou, A. M. CO Adsorption on Transition Metal Clusters: Trends from Density Functional Theory. *Surf. Sci.* **2008**, *602*, 1858–1862.
37. Sun, Y.; Xia, Y. Shape-Controlled Synthesis of Gold and Silver Nanoparticles. *Science* **2002**, *298*, 2176–2179.
38. Macdonald, J. E.; Sadan, M. B.; Houben, L.; Popov, I.; Banin, U. Hybrid Nanoscale Inorganic Cages. *Nat. Mater.* **2010**, *9*, 810–815.
39. Jackson, S. R.; McBride, J. R.; Rosenthal, S. J.; Wright, D. W. Where's the Silver? Imaging Trace Silver Coverage on the Surface of Gold Nanorods. *J. Am. Chem. Soc.* **2014**, *136*, 5261–5263.
40. Kresse, G.; Furthmüller, J. Efficiency of Ab-Initio Total Energy Calculations for Metals and Semiconductors Using a Plane-Wave Basis Set. *Comput. Mater. Sci.* **1996**, *6*, 15–50.
41. Perdew, J. P.; Burke, K.; Ernzerhof, M. Generalized Gradient Approximation Made Simple. *Phys. Rev. Lett.* **1996**, *77*, 3865–3868.
42. Blöchl, P. E. Projector Augmented-Wave Method. *Phys. Rev. B* **1994**, *50*, 17953–17979.
43. Stuckless, J. T.; Al-Sarraf, N.; Wartnaby, C.; King, D. A. Calorimetric Heats of Adsorption for CO on Nickel Single Crystal Surfaces. *J. Chem. Phys.* **1993**, *99*, 2202–2212.
44. Trens, P.; Durand, R.; Coq, B.; Coutanceau, C.; Rousseau, S.; Lamy, C. Poisoning of Pt/C Catalysts by CO and Its Consequences over the Kinetics of Hydrogen Chemisorption. *Appl. Catal., B* **2009**, *92*, 280–284.
45. Shah, V.; Li, T.; Baumert, K. L.; Cheng, H.; Sholl, D. S. A Comparative Study of CO Chemisorption on Flat and Stepped Ni Surfaces Using Density Functional Theory. *Surf. Sci.* **2003**, *537*, 217–227.
46. Ge, Q.; Jenkins, S. J.; King, D. A. Localisation of Adsorbate-Induced Demagnetisation: CO Chemisorbed on Ni$\{110\}$. *Chem. Phys. Lett.* **2000**, *327*, 125–130.
47. Eichler, A. CO Adsorption on Ni(111)−A Density Functional Theory Study. *Surf. Sci.* **2003**, *526*, 332–340.
48. Grechnev, A.; Di Marco, I.; Katsnelson, M. I.; Lichtenstein, A. I.; Wills, J.; Eriksson, O. Theory of Bulk and Surface Quasiparticle Spectra for Fe, Co, and Ni. *Phys. Rev. B* **2007**, *76*, 035107.